Harvesting Energy via Water Movement and Surface Ionics in Microfibrous Ceramic Wools

Manpreet Kaur[a,b*], Avinash Alagumalai[b], Omid Mahian[c,d,e,i*], Sameh M. Osman[f], Tadaaki Nagao[a, g*], Zhong Lin Wang[e,h]

[a]International Center for Materials Nanoarchitectonics (WPI- MANA), National Institute for Materials Science (NIMS), Tsukuba, Ibaraki, 305-0044, Japan

[b]Department of Chemical and Petroleum Engineering, University of Calgary, 2500 University Dr. NW, Calgary, Alberta, T2N 1N4, Canada

[c]Zhejiang Provincial Engineering Research Center for the Safety of Pressure Vessel and Pipeline, Faculty of Mechanical Engineering and Mechanics, Ningbo University, Ningbo 315211, China

[d]Department of Chemical Engineering, Imperial College London, London SW7 2AZ, UK

[e] Beijing Institute of Nanoenergy and Nanosystems, Chinese Academy of Sciences, Beijing, 100083, People's Republic of China

[f] Chemistry Department, College of Science, King Saud University, P.O. Box 2455, Riyadh 11451, Saudi Arabia

[g] Department of Condensed Matter Physics, Hokkaido University, Sapporo, Hokkaido, 060-0810, Japan

[h]School of Materials Science and Engineering, Georgia Institute of Technology, Atlanta, GA, USA

[i] Laboratory on Convective Heat and Mass Transfer, Tomsk State University, 634045, Tomsk, Russia

Corresponding authors: Manpreet (manpreet.kaur7@ucalgary.ca); Omid (o.mahian@imperial.ac.uk; omid.mahian@gmail.com); Tadaaki (nagao.tadaaki@nims.go.jp)

Abstract

Due to the push for carbon neutrality in various human activities, the development of methods for producing electricity without relying on chemical processes or heat sources has become highly significant. Also, the challenge lies in achieving microwatt-scale outputs due to the inherent conductivity of the materials and diverting electric currents. To address this challenge, our research has concentrated on identifying non-conductive mediums for water-

based using low-cost microfibrous ceramic wools in conjunction with a NaCl aqueous solution for power generation. The main source of electricity originates from the directed movement of water molecules and surface ions through densely packed microfibrous ceramic wools due to the effect of dynamic electric double layer. This occurrence bears resemblance to the natural water transpiration in plants, thereby presenting a fresh and straightforward approach for producing eco-friendly electricity. The generator module suggested in this study, measuring 12×6 cm^2, demonstrated a noteworthy open-circuit voltage of 0.35 V, coupled with a short-circuit current of 0.51 mA. Such low-cost ceramic wools are suitable for ubiquitous, permanent energy sources and hold potential for use as self-powered sensors and systems, eliminating the requirement for external energy sources such as sunlight or heat.

Keywords: Energy harvesting; ceramic microfibers; water evaporation; power generation; self-powered systems; clean energy.

1. Introduction

Over the upcoming decades, easily accessible fossil energy resources are anticipated to diminish significantly, exacerbated by their persistent adverse effects on the environmental [1-4]. Recently renewable energy research has advanced to the forefront, and zero-emission energy sources and carbon neutrality have become top priorities in energy research [5-9]. Several devices have been successfully developed utilizing battery-free, self-powered systems, such as piezoelectric or triboelectric nanogenerators [10-12]. Indeed, the concept of self-powered sensors and systems based on "Nanogenerators" was coined by Wang and Song in 2006 [13, 14]. Most such energy-harvesting systems have limitations in regard to operational lifetimes, useful geographic region, or fabrication costs [15, 16]. Also, their nano-fabrication processes are rather demanding and fall far short of meeting industrial needs [17-20]. In recent times, there has been a lot of interest in water-based power generation due to its capacity to harness clean energy stored within the dynamic states of water [21-26]. If the energy absorbed by water could

be harnessed at an efficiency of 1% using water-based power technology, the potential contribution could amount to approximately one-third of the world's energy consumption, which is comparable to the energy output of crude oil [27]. However, this method typically necessitates variations in elevation and is unsuitable for decentralized and widespread energy extraction. In the recent past, innovative nanogenerators that capitalize on water flow have emerged as a solution to overcome this limitation [28-31]. In such devices, electricity generation is based on streaming current, in which an ionic species near the electrical double layer (EDL) at the solid-liquid [32-35] interface carries the electricity during water movement [36-38]. Due to the ample availability of water resources and the increasing requirement for environmentally friendly energy sources, a novel approach has been documented wherein electricity generation is propelled by water. Carbon black, graphene oxide, and carbon nanotubes have been studied together with their hybrid structures[37, 39-45]. However, their achieved voltages have been constrained to millivolt ranges, while their wattage outputs predominantly remain within the microwatt scale. This limitation is likely due to the inherent conductive properties of these materials, which tend to divert the electric currents. To address this challenge, our research has concentrated on identifying non-conductive mediums for water-based power generation. Our focus has shifted towards water transpiration from ceramic media, as we anticipate that these materials hold the potential to deliver higher voltage and power outputs in comparison to systems reliant on carbon-based components. In this work, an endeavor has been made to study the generation of electrical voltage through the process of water transpiration across a ceramic microfiber wool (CW), which acts as an "insulator". This specific ceramic microfiber wool possesses a notable combination of attributes, including a substantial surface area and a multitude of narrow spaces that facilitate capillary forces. Among the numerous options available in the realm of micro-fibrous ceramic materials, CW stands out due to its cost-effectiveness and wide-scale industrial

production. Our previous research demonstrated that the fibrous structure of CW employs capillary action for efficient water evaporation, leading to swift near-room-temperature distillation through solar photothermal evaporation [46]. Building on this, our current study focuses on harnessing the natural movement of water through CW, driven by evapotranspiration, to generate electrical power.

We have utilized commercially available ceramic wool (ISOWOOL Blankets 1260; Isolite Insulating Products Co. Ltd) in our experiments. These ceramic wool products are widely used in refractories for high-temperature equipment and are among the least expensive and most mass-produced industrial materials in this category. The decision to use ceramic fibers with the composition of microfibers comprising 54% SiO_2 and 46% Al_2O_3 was based on their suitable properties for filtration or capillary tasks in corrosive media, elevated temperatures, or pressures. Furthermore, these environmentally friendly and low cost ceramic fibers are flexible, easy to handle, and can be woven into fabrics, allowing for the fabrication of complex-shaped composites.

Through our experiments, we have demonstrated that surface-modified CW serves as a proficient power generator fabricated using a device measuring 12×6 cm^2. Furthermore, we explored the potential for voltage scaling by arranging such devices in series, leading to an impressive voltage increase to 1.6 V. This level of voltage proves adequate for tasks such as charging a supercapacitor to illuminate an LED or operate a motorized fan.

A remarkable advantage of this system is its fuel source – ionized water, which is naturally evaporated, can serve as the generator's fuel. Consequently, this generator can operate continuously, both during the day and night. This unique trait positions it as a valuable power supply for self-sustaining systems, thereby complementing the operation of solar cells.

2. Methods

Initially, the CW underwent a cleaning process using a sodium hydroxide solution. To transition the hydrophobic nature of CW to hydrophilic, hydroxyl (OH) groups were introduced through the reaction with sodium hydroxide. The negative zeta potential indicates the negative charges due to OH groups on the modified CW surface. In all measurements, this OH modified hydrophilic CW was used, and the narrow spacing in between the fibers induced a capillary force that resulted in efficient uptake and transpiration of water by this material.

Figure 1 provides an overview of the entire apparatus and experimental arrangement employed to measure the electric potential generated through evaporation. To fabricate the ceramic wool electric generator (CWEG) device, two cotton sheets measuring 12×6 cm^2 each were prepared. Subsequently, 1,000 mg of CW was reshaped into a thin layer measuring 12×6 cm^2 with a thickness of approximately 0.2 cm. This CW layer was then placed between the two cotton sheets, and this assembly was further enclosed between two plastic grids as depicted in Figure 1(a-i). The entire structure was secured using plastic clamps to fasten the electrodes in place. The electrodes were copper plates or carbon-glass plates (Figure 1e and 1h). To simplify the handling of the CWEG device, copper (Cu) plates were utilized as electrodes in all conducted experiments. This device, with the Cu electrodes, was positioned within a beaker to facilitate the measurement of the potential variation across the CWEG sample.

The employed CW comprised microfibers which exhibited an average diameter of around 3.2 µm (as depicted in Figure 1j). By utilizing the Brunauer–Emmett–Teller method, the specific surface area of the CW was determined to be 70.99 m^2g^{-1}. Additionally, electrical connections were established using two electrical clamps. Graphite paste was used to safeguard the electrode. This paste-coated area was subsequently dried at a temperature of

50 °C for a duration of 3 hours. This measure was undertaken to prevent corrosion within a 2 mM saline environment. **Figure S1** shows (a) Prior to and (b) Post graphite coating effect pictures of the electrode.

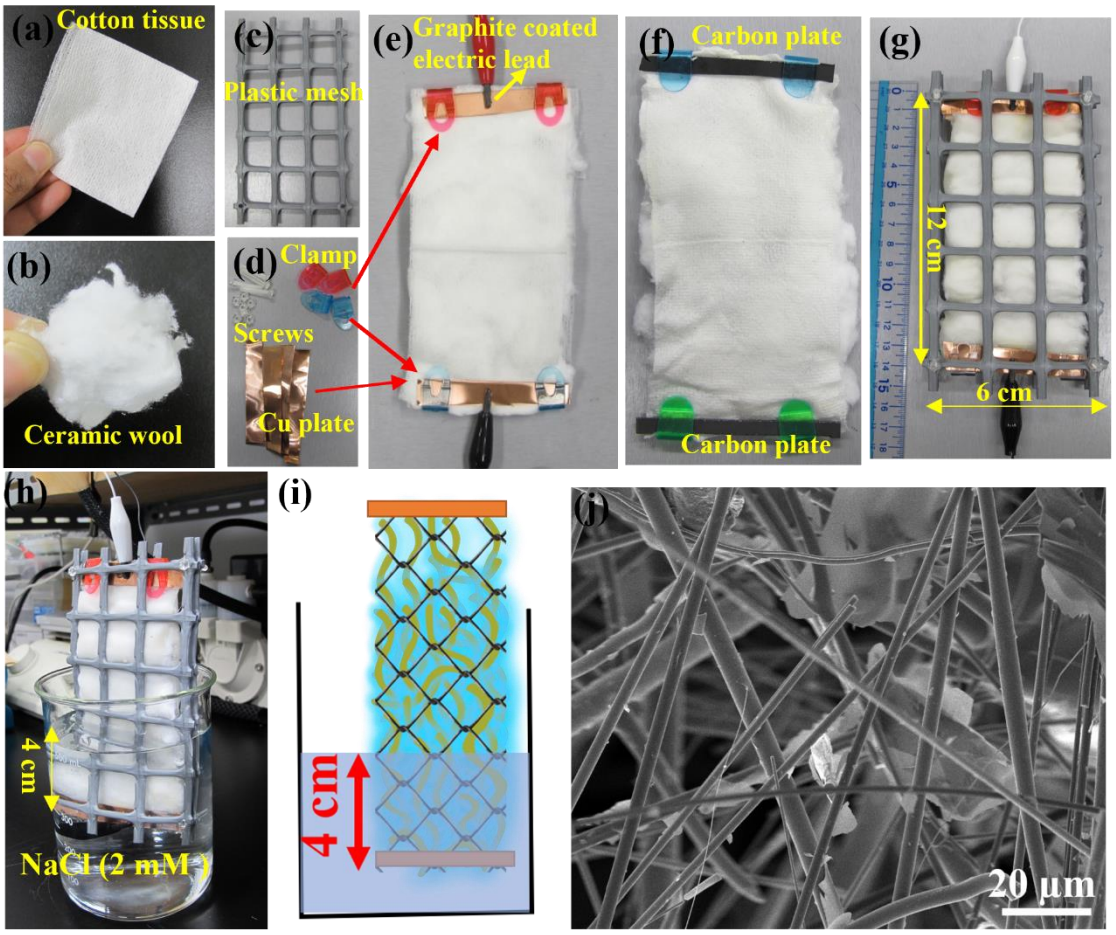

Figure 1. Design of a ceramic wool electric generator (CWEG) (a) commercial grade cotton fiber cloth (b) ceramic wool (CW) (c) plastic grid (d) plastic clamp, plastic screw, and Cu plates (e) prepared CWEG (f) prepared CWEG using carbon glass plate (g) CWEG in a grid (h) complete CWEG setup in NaCl (i) schematic diagram of the setup for current-voltage measurement (j) SEM of CW.

The CWEG was introduced to a 2 mM NaCl aqueous solution. This solution covered a 4 cm segment of the CWEG, while the rest remained exposed to the surrounding atmosphere (depicted in Figure 1i). One of the electrodes positioned at the extremity of the CWEGs was submerged in the water. The water infiltrated to a level several centimeters above the water

surface in the beaker due to capillarity effect of filler. This capillary effect emulates the water transpiration observed in plants.

The energy conversion performance of the CW device was determined using a VersaSTAT potentiometer (VersaSTAT 4, Princeton Applied Research) under water evaporation. Before the measurements, the fibers were readied with the NaCl solution for almost 1 h. All tests were performed thrice to determine their repeatability. The following are the CWEG dimensions; ~ 12 × 6 cm^2, thickness ~0.2 cm, weight ~1 g (optimized CWEG dimensions and discussed below), followed by all other experiments in this work. The voltage and current values with the mean and standard deviation of five devices is shown in Table S1.

3. Results and Discussion

The working principle of the evaporative nanogenerator is shown in **Figure 2**. Wang et al.'s research underscores the primary involvement of electrons in the initial formation of the charge layer during the phenomenon of liquid-solid contact electrification, commonly referred to as triboelectrification [47-49]. The nanogenerator, which relies on water evaporation, utilizes this phenomenon for mechanical energy harvesting and investigating charge transfer at these interfaces. These nanogenerators operate by combining contact electrification and electrostatic induction, entailing surface electron/ion/material transfer and generating electric potential differences upon separation in materials with contrasting triboelectric polarity [50, 51]. Ceramic fibers possess several desirable qualities over the previous used nanogenerators materials, rendering them appealing for filtration or capillary applications in corrosive environments, high temperatures, or under elevated pressures.

Measured zeta potential values (discussed later) are well aligned with the origin of the evaporation induced streaming potential and chemistry of NaCl on the CW surface. The zeta potential values give an indication of the negative charge on the modified CW surface. The

noticeable hydrophilic characteristics of CW, attributable to the presence of surface -OH groups (as confirmed by zeta potential values), facilitate the deep penetration of water molecules into the interior of the CWEG. As a result, the water adsorbed by the hydrophilic nature of CW promptly wets the surface, consequently triggering surface charging. Notably, during the measurement, the bottom CWEG electrode functions as the negative electrode, while the top electrode serves as the positive electrode.

In the aqueous environment, the presence of ions initiates the development of an interfacial charge layer that closely resembles an EDL when these ions interact with the hydroxyl (OH) groups situated on the ceramic fibers. Counterions, such as Na^+, exhibit a distinct preference for upward migration within the mobile layer of the EDL due to the capillary-induced pressure gradient [52]. This upward migration ultimately leads to the creation of charge polarization, subsequently giving rise to the generation of an induced streaming potential. Chemically, this is due to the dynamic electric double layer, which is produced by the change in liquid covered surface area and/or ion migration at the vicinity of the surface due to charge transfer between liquid and solid [49]. The structure of the Capillary-Woven CWEG doesn't inherently possess pores, but rather its porosity arises from the interstitial spaces between the crisscrossed fibers. When an electrolyte solution flows through such a capillary or porous medium with narrow spaces, comparable to the Debye length of the fluid, counterions tend to occupy these spaces due to the overlapping EDLs.

In summary, upon inserting the CWEG into NaCl solution, contact electrification occurs, resulting in the negatively charged CW walls and the spontaneous formation of an EDL at the interface between the CW fibers and the surrounding water. This process is notably facilitated by the combined influences of capillary forces and evaporation. The measured zeta potential of CW is -49.09 mV. To maintain charge neutrality at the CW-NaCl interface, negatively

charged CW walls attract cations (Na^+), while excluding anions (Cl^-), creating the EDL. As water flows, these ions move upward with it. In evaporation-driven flow, the EDL generates a net positive charge transport, creating a streaming current and inducing a streaming potential. This potential difference between CWEG electrodes drives a continuous unidirectional electron flow, resulting in a conduction current.

Considering the complex fibrous CW architecture, numerous electrochemical reactions likely occur on the electrodes during the passage of current. However, for clarity, a generalized schematic illustrates electron movement from the induced cathode to the anode (Figure 2b).

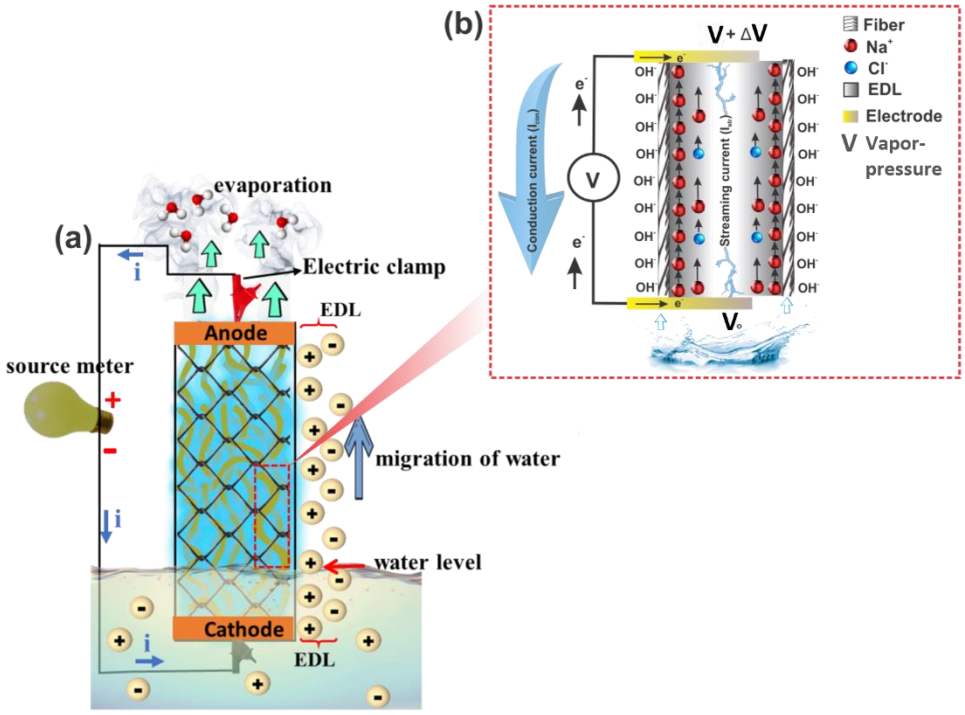

Figure 2. (a) Schematic representation of the experimental setup for measuring induced potential and (b) capillary transport of ions on individual fiber, showing the specific ion distribution on the fiber.

A modified hydrophilic CW with intricate fibers generates an electric potential difference between integrated electrodes as liquid flows through it. This potential difference increases

until reaching its peak. When dry, no open-circuit voltage (Voc) is observed, but when saturated with a 2 mM NaCl solution, a Voc of 0.35V arises after about an hour, as water reaches certain height, indicating material and solution properties influence this voltage generation (**Figure 3a)**. A similar experiment was performed with a carbon-glass plate electrode (**Figure S2),** which gives nearly the same result as Cu-plate electrodes, indicating that the redox reaction of Cu electrodes is not the main source of voltage generation. A 1-μF capacitor charges to 0.35 V in 10 min (Figure 3a, inset). Throughout all experiments, the CWEG device maintains an angle of approximately 60° with respect to the water surface within the beaker. This orientation permits the water to ascend to a height of roughly 4 cm above the water level. Variations in the measured voltage can be attributed to the oscillations in laboratory temperature and humidity during the testing period. Additionally, the suggested model shows that the generated electricity can be significantly amplified by series connection (Figure 3b). V_{OC} increases linearly, with slight variations due to losses stemming from wiring and contact resistance. Two, three, and six samples in series can produce up to 0.61 V, 0. 90 V, and 1.61 V, respectively.

Nonetheless, the induced voltage remains consistently close to 0.35 V during the entirety of a 6-hour test, while the short-circuit current (Isc) maintains a stable value of around 0.5 mA as presented in **Figure S3**. This dependable performance occurs within a laboratory environment characterized by temperature variations, along with relative humidity (RH) levels spanning from 45% to 55%. The initial variations in the readings can be attributed to the swift advancement of the capillary front. This front eventually stabilizes as a balance is achieved between water adsorption and evaporation processes. The open-circuit voltage (Voc) and short-circuit current (Isc) are 0.35 V and 0.5mA, respectively (Figure 3c). The completely dried sample before adding water into beaker shows essentially zero current.

Submerging the CWEG in water leads to the manifestation of an IV curve with a discernible slope and an offset.

Figure 3d shows that the zeta potentials of pristine and modified CW are 8.15 ± 0.035 mV, and -49.09 ± 0.215 mV, respectively, where each sample was measured 3 times and presented the mean and standard deviation values. The negative zeta potential indicates the negative charges due to OH groups on the modified CW surface [53]. Measured zeta potential values are well aligned with the origin of the evaporation induced streaming potential and chemistry of NaCl on the CW surface as presented in **Figure 2**. The zeta potential values give an indication of the negative charge on the modified CW surface.

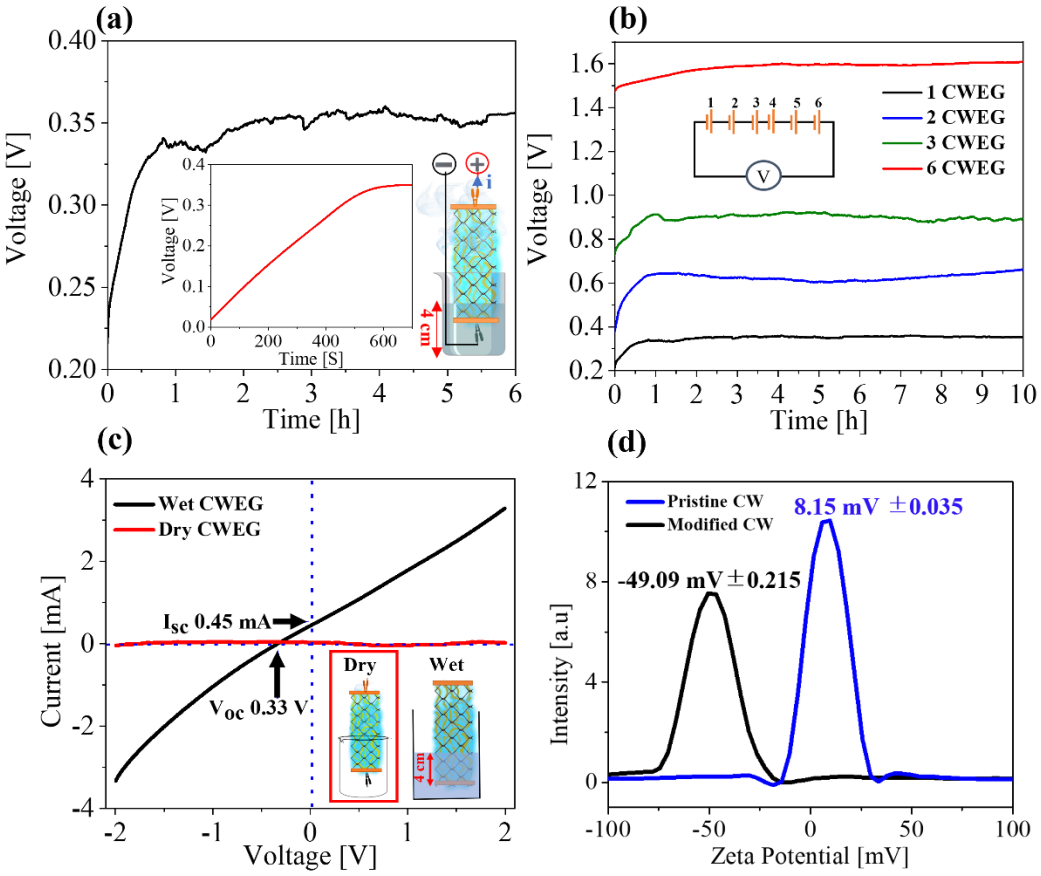

Figure 3. Electrical attributes of the CWEG device: (a) Voltage generated by a CWEG over time (in hours), while it is immersed to a depth of 4 cm in NaCl solution, (b) Voltage generated by 1 to 6 CWEG devices in series mode, (c) The Performance of CWEG devices in both dry and saturated

states within the ambient environment and (d) Zeta potential variations of pristine CW and modified CW

Further insights into the generation of streaming potential come from additional experiments using NaCl solution with different degrees of immersion of the CWEG in water (**Figure 4a**). The bottom electrode of the nanogenerator was kept under the water, and the top electrode was kept above it. For water depths of 1, 2, 3, 4 and 5 cm, voltages of the device were 0.27, 0.31, 0.33 0.35, and 0.34 V, respectively. The maximum voltage was observed, when the CWEG was inserted 4 cm into the water, beyond which it decreased. With further increases in the water level, the evaporation zone diminished, and the voltage decreased. Therefore, placing the air-water interface near the middle of the CWEG is essential for voltage generation, which effectively promotes evapotranspiration through the fibrous media.

On the other hand, to optimize the effect of device size on performance of the device, we conducted an experiment with three different sample sizes. We first used a 6 x 6 cm^2 device which showed 0.24 V. To increase the device performance further, we increased the length of the device to 12 x 6 cm^2 and achieved 0.35 V. We then increased the width of the device to 12 x 12 cm^2, which further increased the voltage to 0.38 V (Figure 4b). Hence, voltage generation increases with increasing CWEG area. We chose 12 x 6 cm^2 for the rest of our measurements for ease of device setup in a laboratory beaker.

Next, we optimized the mass of CW sandwiched between the cotton tissues in Figure 4c and Note S1. We tested voltage generation performance using cotton tissue without CW and the voltage for cotton tissue only was considerably lower (0.012 V) than for the CW sandwich. By sandwiching 500 mg of CW between cotton (~ 35 mg/cm^3), we achieved 0.17 V, which increases with higher amounts of CW, up to a maximum of 1000 mg (~ 69 mg/cm^3), beyond which the voltage actually decreased slightly. The higher CW fiber density (number of fibers per unit length) increases the pore density, leading to higher device performance. However,

increasing the fiber density further increases the flow resistance, reducing the amount of evaporation. Therefore, to avoid the excess spun fibers, which diminishes the spacing efficiency of fibers, impeding ion migration, we have chosen 1000 mg CW weight (~ 69 mg/cm^3) for the remaining measurements.

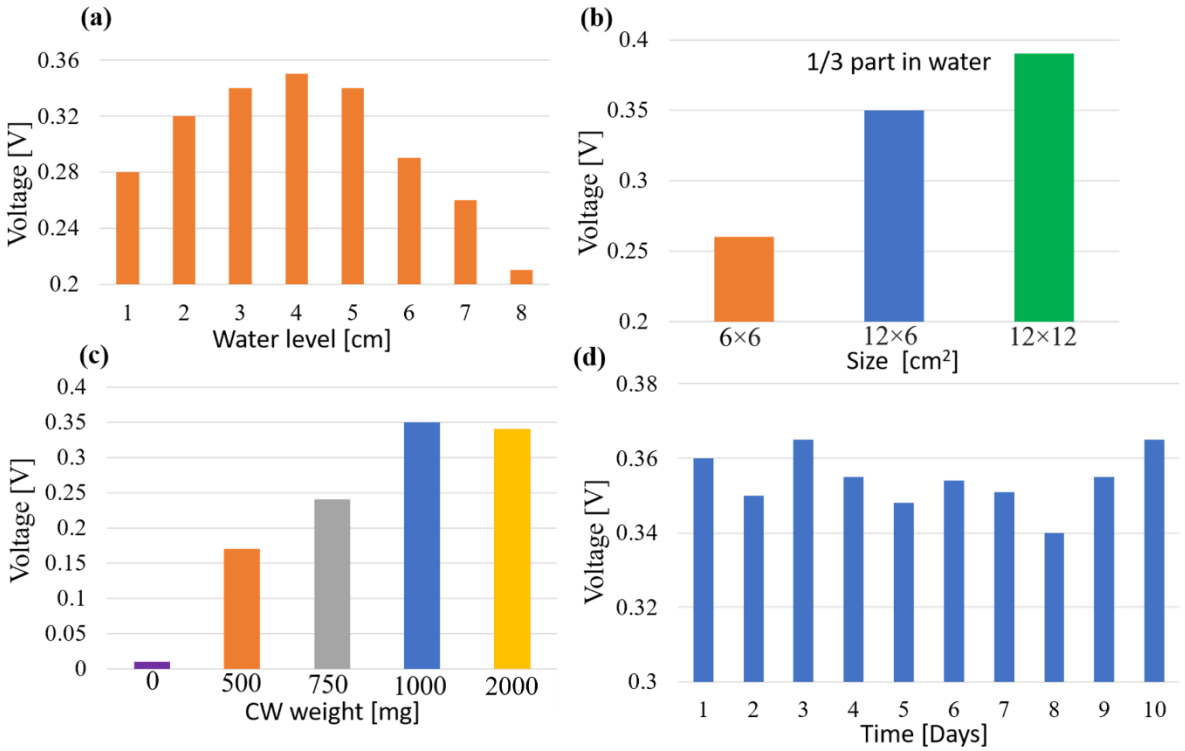

Figure 4. Voltage generation performance of CWEG with different (a) water levels (cm), (b) sample sizes, (c) CW masses sandwiched between cotton tissues, and (d) voltage generated continuously by a CWEG for 10 days, in which each cycle represents 8 hours of measurement every day.

To assess the extended stability of the device, we conducted measurements continuously for 10 days, each day spanning 8 hours (Figure 4d). Notably, the recorded voltage exhibited remarkable stability over this time frame. Throughout the course of the 10-day experimentation period, the device's performance remained nearly constant, with only marginal fluctuations in readings. These fluctuations can be attributed to alterations in ambient conditions. Consequently, the device can be regarded as a "micro 'green' power plant" capable of providing a consistent power supply with virtually negligible energy input.

Comparative studies on water evaporation were performed using CWEGs and NaCl solution. Evaporation of water was tested using an electric balance (AUW220D, Shimadzu). The amount of NaCl solution was fixed at 100 mL (1 $\times 10^5$ mg), indicating the high evaporation efficiency of the CWEG as compared with a beaker containing only saline (**Figure 5a**). After 3,600 s, the water mass loss with the CW reached 2250 mg. Therefore, due to high evaporation efficiency of the CWEG, we have observed voltages as high as 0.35 V with high stability from a 12 x 6 cm^2 device.

In order to further confirm the directional nature of the voltage generation, we exchanged the electrical leads, resulting in a change in polarity (Figure 5b). Upon reversing the connections, the voltage's sign also reverses, yet it retains the same magnitude. This observation leads us to the conclusion that the voltage's direction is contingent upon the direction of water flow induced by evaporation (Figure 5b).

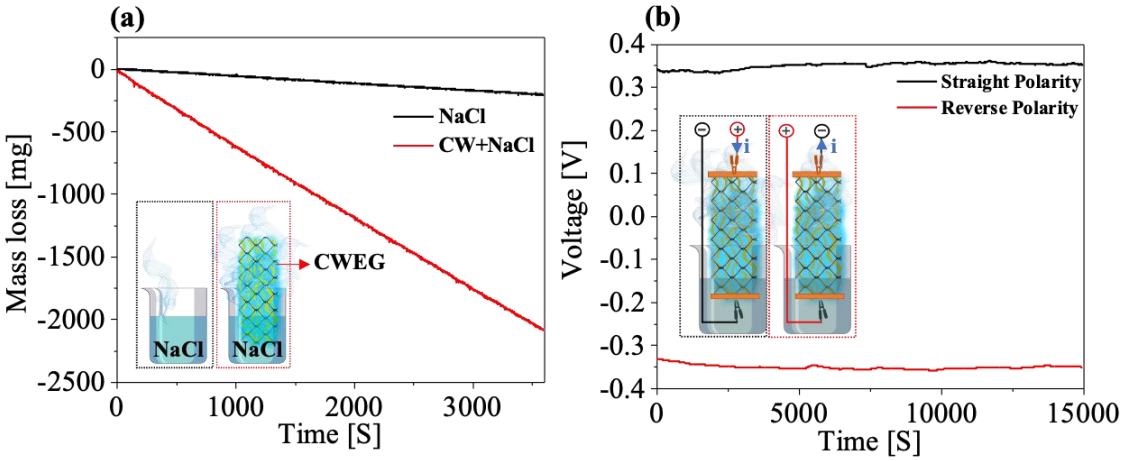

Figure 5. (a) Evaporation is significantly greater with a CWEG device than without. (b) Induced potential for CWEGs connected in normal and reversed polarity (inset schematic shows sample setup).

We conducted a comprehensive experiment to explore the relationship between induced potential and pH value (electrolyte concentration). This involved systematically adjusting the electrolyte concentration or pH value and measuring the corresponding voltage responses.

Three different electrolyte concentration solutions were prepared: a 0.2 mM NaCl aqueous solution with a pH of ~7, a 2 mM NaCl aqueous solution with a pH of ~6 due to the increased concentration of NaCl, and a 20 mM NaCl aqueous solution with a pH of ~5, reflecting a further decrease in pH with increasing NaCl concentration. The induced voltage increased initially as the NaCl solution molarity increased from 0.2 to 2 mM (**Figure 6a**). However, when considering the 0.2 mM solution, the significantly low number of ions present might not favor efficient surface ionization, leading to a diminished induced potential. In contrast, the greater ion density in a 2 mM solution significantly enhances the voltage output, nearly 1.5 times greater compared to the 0.2 mM solution. Peculiarly, further elevating the ionic concentration from 2 to 20 mM yields only minimal effects on the induced voltage. This phenomenon can be comprehended through conventional electrokinetic theory. As the concentration of the electrolyte rises, the thickness of the EDL diminishes. This outcome leads to a reduction in the potential. [54, 55].

The electrolyte solutions of different composition such as NaOH solution, tap water, distilled water, and ethanol were examined whether intrinsic properties of the liquid can affect the performance of the CWEG device. Furthermore, Principal Component Analysis (PCA) was applied to electrolyte solutions based on voltage and conductivity variables to gain valuable insights (**Figure S4**). This analysis was conducted to clarify how these electrolytes interrelate concerning their electrical and conductivity traits, revealing distinct behaviors for NaOH, different water types, and ethanol. A positive correlation is observed in the case of the NaOH electrolyte solution, indicating heightened electrical activity. Notably, tap water and distilled water fall within the same quadrant, suggesting their similarity in terms of voltage and conductivity attributes within this specific feature space. The juxtaposition of positive and negative values in the first and second components respectively underscores the intricate

influence of NaCl on the voltage and conductivity data. In contrast, ethanol showcases negative scores, signifying its distinct impact on the data's variability.

The induced potential (Figure 6) for different solutions varies in the following manner: NaCl > NaOH > tap water > distilled water > ethanol, with voltages of 0.35, 0.21, 0.15, 0.11, and 0.06 V, respectively. The tap water was taken from the Tsukuba, Japan municipal water supply. NaCl samples generate much higher voltage values due to the high ion concentration. On the other hand, a low-polarity ethanol solution does not exhibit a strong EDL due to its relatively low concentration of hydrogen protons. As a consequence, the resulting voltage is lower. It's worth highlighting that the streaming potential is notably more pronounced in a NaCl solution. A clear correlation is seen in the difference of measured conductivity, which affects the ability to respond to the moving EDL boundary.

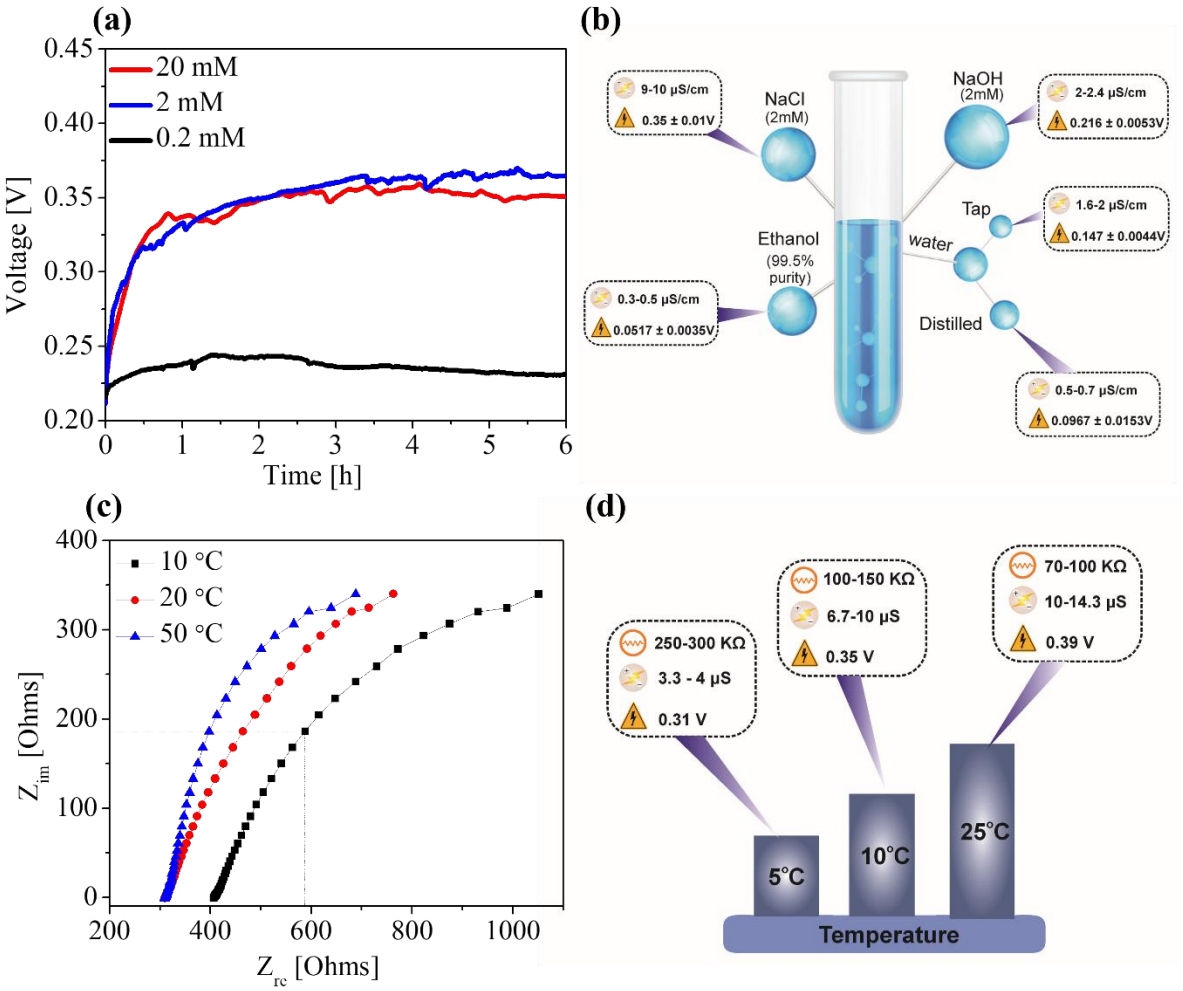

Figure 6. (a) Voltage generation with respect to electrolyte concentration, (b) mean values of voltage generated from variety of electrolyte solutions and their conductivity data, (c) Effect of temperature on device performance shown by Nyquist plot (d) Values for resistivity, conductivity, and voltage with respect to temperature.

The charge carrier dynamics occurring at the interface between the CW and the electrolyte can be characterized through the application of electrochemical impedance spectroscopy (EIS). The electrochemical performance of the CWEG was studied using a NaCl electrolyte in a two-electrode EIS system [56]. In Figure 6 (c), Z_{im} and Z_{re} represent the imaginary and real components, respectively, of the impedance (Z) as a function of frequency. Impedance is a complex quantity that describes the opposition to the flow of an alternating current in a circuit. Z_{im} (Z imaginary) refers to the imaginary component of the impedance, which

represents the reactive part of the impedance. It is associated with the capacitive or inductive elements in the system and is typically plotted along the vertical axis of a Nyquist plot. Z_{re} (Z real) refers to the real component of the impedance, which represents the resistive part of the impedance. It is associated with the resistive elements in the system and is typically plotted along the horizontal axis of a Nyquist plot.

In the context of Figure 6(c), the Nyquist plot displays the alteration of impedance (|Z|) as a function of frequency, with Z_{im} and Z_{re} providing insights into the reactive and resistive components of the impedance, respectively. The diameter of the semicircle within the Nyquist plot serves as an indicator of the charge transfer resistance from the CWEG to the electrolyte, particularly in relation to the temperature of the NaCl solution.

The apparent trend indicates that higher temperatures substantially enhance charge transfer efficiency. This is evidenced by the smaller arc observed at higher temperatures in comparison to the arc displayed at lower temperatures (Figure 6c). This finding underscores that the acceleration of charge transfer is markedly achieved through elevated temperatures. As the temperature decreases, voltage also decreases due to a decrease in conductivity of the NaCl solution (Figure 6d). The maximum V_{OC} is recorded as ~0.39 V at 50 °C, where the effects of temperature and water evaporation raise the generated voltage significantly. The performance of the device experiences a gradual decline from its optimal state as the electrolyte temperature diminishes. This deterioration continues until it reaches a minimum value of ~0.31 V at a temperature of around 10 °C. Hence, the water temperature around the CWEG influences the capacity of power generation. These results suggest that the CWEG would be most effective at producing electric energy in warm, dry environments.

Additionally, to realize the influence of temperature and water evaporation on the device's performance, we conducted an additional comparison under concentrated 100-mW cm^{-2}

sunlight, utilizing a solar simulator (**Figure 7a**). The voltage increased and decreased as the solar simulator was turned on and off, respectively. During illumination, CW absorbs light and due to photothermal heat generation, evaporation is enhanced, leading to an increase in voltage. The voltage returns to a low value after the light is turned off; thus the combined effect of solar heating and evaporation is clearly beneficial.

Subsequently, in order to ascertain that evaporation indeed serves as the primary source of the induced potential, the top surface of the CW was subjected to moving air at ~2 m/s (with a temperature of around 22 °C). Air movement enhanced the evaporation rate from the CW, leading to a slight increase in voltage up to ~0.36 V (Figure 7b). Upon ceasing the airflow, the induced potential decreased to ~0.35 V. This clear correlation between the output voltage and the rate of water evaporation underscores the significance of this process. Subsequently, the behavior of the streaming voltage performance was further explored through the controlled removal and injection of water (Figure 7c). The beaker was initially filled with water so that the CWEG was immersed 4 cm. Then, after a few seconds, when all water was removed from the beaker, voltage quickly dropped to ~0.13 V. The voltage difference started to increase again and reached the maximum and stabilized with further water addition. This behavior was highly reproducible.

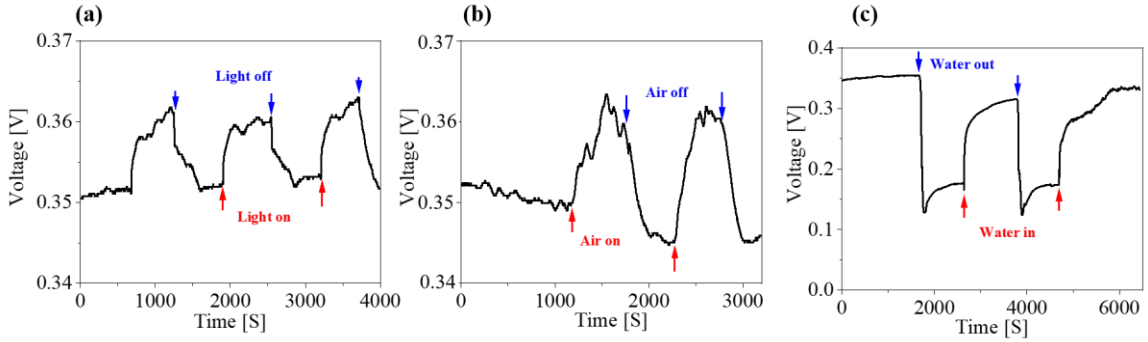

Figures 7. Device performance in different ambient conditions. Effect of induced potential on periodic application of (a) simulated solar light (b) air flow (c) ejecting and injecting water.

In this work, we also studied the effect of surface modification with an ultrathin TiO_2 coating on the CW fibers (CW-TiO_2). A uniform 20-nm TiO_2 coating was deposited on CW fiber surfaces by atomic layer deposition (ALD) for a comparative study. The TiO_2 coating was annealed at 300 °C for 3 h after deposition. Microscopic morphology of the CW-TiO_2 was inspected with scanning electron microscopy (Hitachi FE-SEM SU8230) and EDX (**Figure 8**). SEM data show that CW-TiO_2 comprises fibers with a diameter of about 5 µm (Figure 8a). The EDX spectrum (Figure 8b), indicates peaks of O, Al, Si, and Ti and EDX mapping confirms the presence of TiO_2 on CW fibers. A carbon peak appears due to the supporting carbon tape holding the sample. The overall morphology of CW-TiO_2 reveals successful coating of TiO_2 on the CW. Crystallinity of the samples was characterized with X-ray diffraction (XRD, RINT 2000, Rigaku). All peaks are indexed to the anatase phase of TiO_2 (JCPDS card No. 21-1272). The diffraction pattern of the CW exhibited a broad feature at 2 theta - 23°, corresponding to amorphous SiO_2 and Al_2O_3 structures[57] (**Figure S5a**). However, after the CW surface modification with TiO_2, the XRD pattern of the CW-TiO_2 exhibited sharp peaks corresponding to TiO_2 NPs. From the Nyquist plot (Figure S5b), it is clear that TiO_2 coating exhibits a notable increase of charge transfer efficiency, resulting in a smaller arc than that of bare CW, which means that charge transfer is drastically enhanced by TiO_2 NPs. The maximum short-circuit current density (J_{max}) for CW and CW-TiO_2 was found to be 0.51 mA and 0.82 mA, respectively, while the corresponding open-circuit voltages (V_{max}) were 0.35 V and 0.30 V, respectively (Figure S5c-S5d). Utilizing the formula $P_{max} = J_{max} \times V_{max}$, where P_{max} represents the maximum output power density, we calculated the power densities for CW and CW-TiO_2 to be 0.18 mW and 0.25 mW, respectively, based on a sample size of 12×6 cm^2. Although the voltage decreased with the TiO_2 coating, the higher current density resulted in a significant increase in the overall power density. This observation indicates that while the TiO_2 coating may lead to a reduction in voltage, it concurrently

enhances the current output, thereby improving the overall power generation performance of the CWEG.

Hence, the substantial increase in power output with the TiO_2 coating demonstrates the potential for strategically improving CWEG performance through surface modifications with appropriate materials.

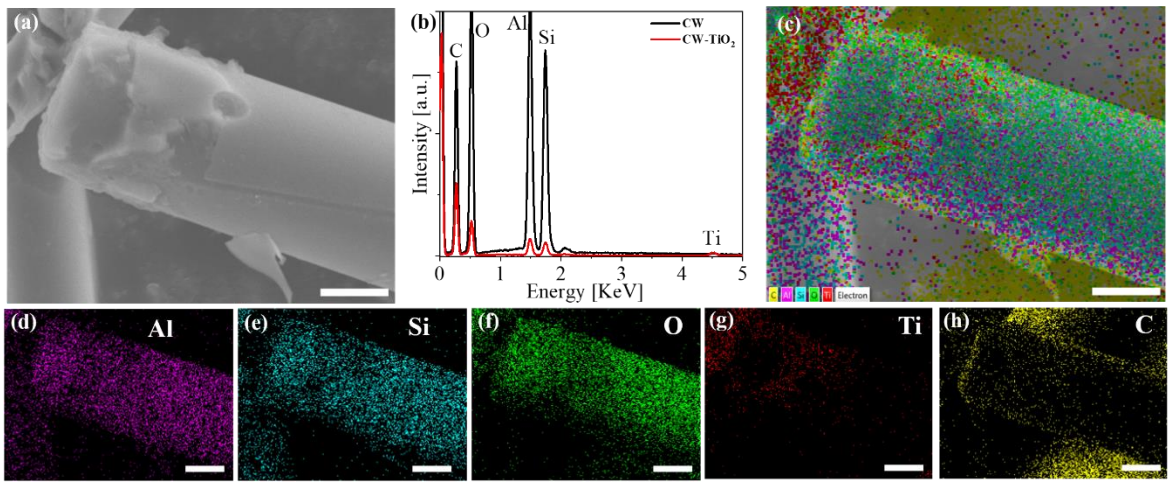

Figure 8. EDX mapping of CW-TiO_2, (a) SEM image, (b) EDX spectrum of CW and CW-TiO_2, (c), (d), (e), (f), (g) and (h) elemental mapping of Al, Si, O, Ti and C (scale bar represents 2 µm).

The evaporative nanogenerator is capable of generating direct current (DC) electricity, which can be harnessed and stored in flexible supercapacitors. These supercapacitors can subsequently be interconnected to meet the energy demands of diverse electronic devices, effectively providing power for various applications. **Figure 9** depicts the capillarity-coupled, evaporation-induced voltage generated by a series of 6 CWEGs, yielding a maximum potential of around 1.6 V. The configuration of these 6 CWEGs, along with the measurement setup, is detailed in Figure 9. The power derived from these devices can be utilized to illuminate a red LED, as demonstrated in **Figure S6**. Notably, the generated electricity is scalable by employing devices in series, enabling it to charge a 1-µF capacitor to 1.5 V

within a 4-hour timeframe using 6 devices in series (**Figure S7**). The energy stored through this process proves sufficient to maintain the illumination of a red LED at a substantial intensity for over 1 hour and to power a small DC motor for a duration of 50 seconds (Video S1). The comparison of CWEG's electrical performance with latest water evaporation-based power devices is presented in Table S2.

The outcomes of these experiments indicate that the proposed CWEG has the capacity to generate sufficient power to operate small-scale electronic devices like LEDs, capacitors, and micro motors. A single CWEG, measuring 12 × 6 cm^2, can produce approximately 0.35 V.

Furthermore, the overall output performance of the system can be maximized through proper selection and matching of load impedance as the real world application involves variable or unpredictable load applied to the energy harvesters[58, 59].

As the CWEG with size of 12 × 6 cm^2 can generate ~ 0.35 mV which is slightly more than the standard redox potential of copper [60]. Thus, the redox reactions did not occur on the copper electrodes actively. However, the redox reaction can adversely influence long-term practical application of the series-connected CWEG system [61]. It's worth considering that such redox reactions could potentially hinder the long-term practical application of series-connected CWEG devices.

The implications of these findings are significant, suggesting the potential application of micro-structured insulating materials for electricity generation. Moreover, the comparison with reported phenomena, such as a single droplet lighting up LEDs or powering a light bulb [62], highlights the remarkable efficiency of water evaporation-based electricity generation.

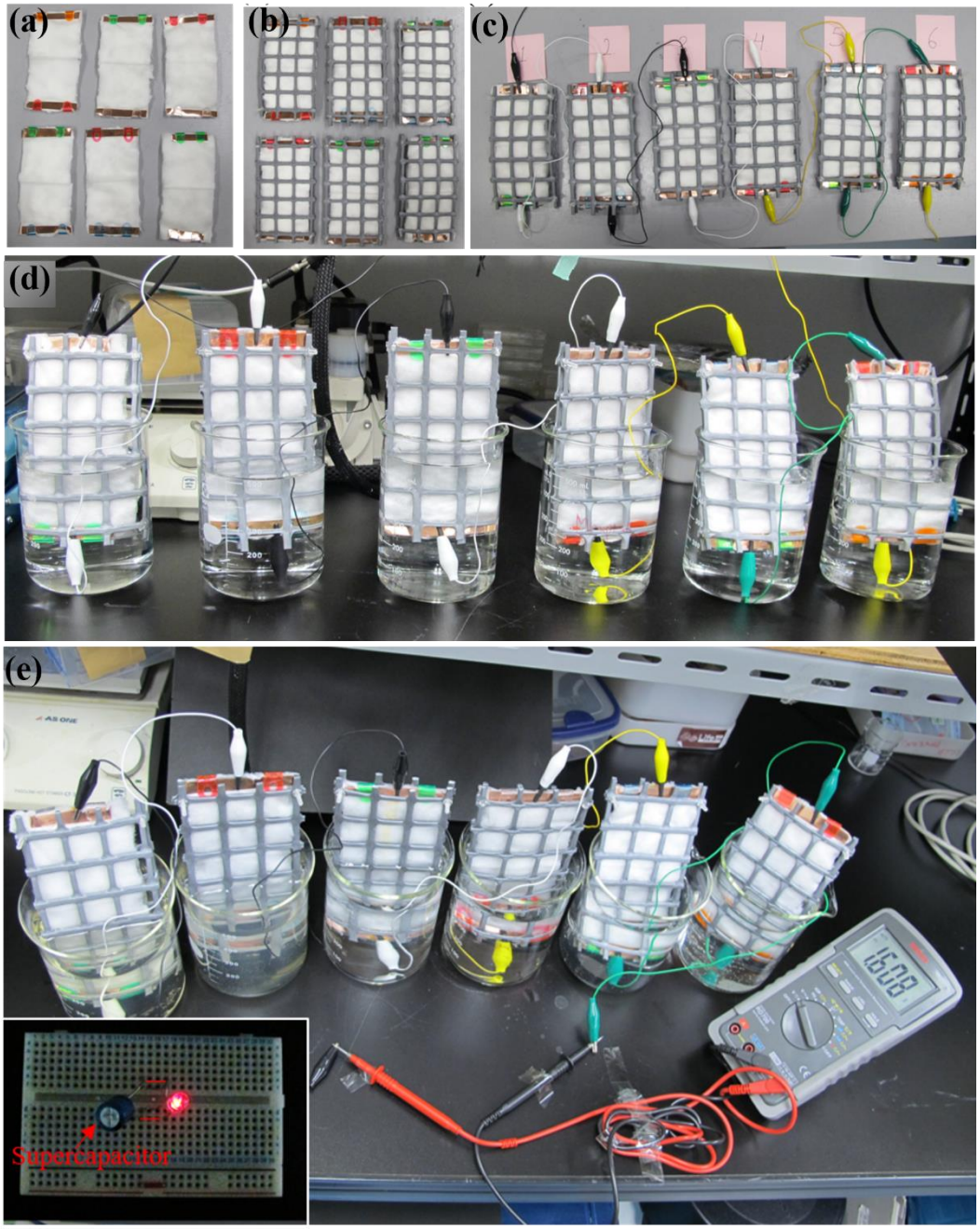

458

459 **Figure 9.** Six CWEG devices (a) as prepared (b) in scaffolds (c) connected in series (d)
460 connected in electrolyte solutions. (e) Scaling of CWEG performance and its use to power an
461 LED by charging of a commercial 1-µF supercapacitor. The inset shows a glowing LED
462 driven through a charged supercapacitor.

463

464

4. Conclusion

This research demonstrates a successful utilization of water's evaporative energy to create straightforward, economical devices for producing clean and sustainable power. The investigation demonstrates that the evaporation of ionic water from ceramic fibers generates electric voltages, and remarkably, the Voc remains stable as long as the device is partially immersed in water. Notably, the voltage resulting from evaporation effects can be extended to around 1.6 V by connecting 12×6 cm^2 CWEGs in series

These CWEGs offer an environmentally friendly solution by utilizing water for power generation. The unidirectional water movement, akin to transpiration, propels efficient charge transfer. This dynamic yields a voltage drop between the two electrodes that are asymmetrically positioned in water and air environments. This difference in environments can also result in additional chemical potential difference.

Our results imply that a bundle of proposed CWEG can generate sufficient power for operating commercial electronic devices. The results reported here demonstrates the great potential for adopting micro-structured insulating material for generating electricity for night-time self-powered LEDs, capacitors, micro motors and household minigadgets, environmental sensors, and so forth. This approach can improve the contact electrification effect and its energy conversion efficiency in practical applications. Such low-cost ceramic wools are suitable for self-powered sensors and systems that do not rely on input sources, such as sunlight and heat.

In forthcoming research, our primary focus will be on addressing the redox reaction issue. We plan to develop redox reaction-free electrodes to ensure the practical viability of the CWEG system over extended operational periods. One future direction is to consider the use

of polymer meshes coated with conductive carbon materials to create electrodes that can mitigate or eliminate these redox reactions.

ASSOCIATED CONTENT

Supporting Information. Figures S1-S7, Table S1-S2, Note S1 and Video S1.

Funding Sources

This work was funded by JSPS KAKENHI (16H06364) and CREST "Phase Interface Science for Highly Efficient Energy Utilization" (JPMJCR13C3) from the Japan Science and Technology Agency.

Acknowlegements: We would like to thank Dr. Takemura Taro, Miss Li Xianglan from the Molecules and Materials Synthesis Platform, NIMS for Zeta Potenial measurment support. The authors extend their appreciation to the Deputyship for Research and Innovation, "Ministry of Education" in Saudi Arabia for funding this research (IFKSUOR3-615-1). O.M. would like to thank the support of Tomsk State University Development Programme (priority-2030) for this work.

References

1. H. J. Hovel, *NASA STI/Recon Technical Report A*, 1975, **76**.
2. C. J. Brabec, N. S. Sariciftci and J. C. Hummelen, *Adv. Funct. Mater.*, 2001, **11**, 15-26.
3. I. Katsouras, K. Asadi, M. Li, T. B. Van Driel, K. S. Kjaer, D. Zhao, T. Lenz, Y. Gu, P. W. Blom and D. Damjanovic, *Nature materials*, 2016, **15**, 78.
4. Y. Zi, J. Wang, S. Wang, S. Li, Z. Wen, H. Guo and Z. L. Wang, *Nat Commun.*, 2016, **7**, 10987.
5. C. F. Maduko and U. B. Akuru.
6. R. Newell, D. Raimi and G. Aldana, *Resources for the Future*, 2019, 8-19.
7. A. M. Omer, *Renewable and sustainable energy reviews*, 2008, **12**, 1789-1821.
8. C. Okkerse and H. Van Bekkum, *Green Chemistry*, 1999, **1**, 107-114.
9. O. Ellabban, H. Abu-Rub and F. Blaabjerg, *Renewable and Sustainable Energy Reviews*, 2014, **39**, 748-764.
10. V. Slabov, S. Kopyl, M. P. Soares dos Santos and A. L. Kholkin, *Nano-Micro Letters*, 2020, **12**, 1-18.
11. K. Zhao, Y. Wang, L. Han, Y. Wang, X. Luo, Z. Zhang and Y. Yang, *Nano-Micro Letters*, 2019, **11**, 1-19.

12. J. Yi, K. Dong, S. Shen, Y. Jiang, X. Peng, C. Ye and Z. L. Wang, *Nano-micro letters*, 2021, **13**, 1-13.
13. Z. L. Wang and J. Song, *Science*, 2006, **312**, 242-246.
14. F.-R. Fan, Z.-Q. Tian and Z. L. Wang, *Nano energy*, 2012, **1**, 328-334.
15. A. J. Williams, M. F. Torquato, I. M. Cameron, A. A. Fahmy and J. Sienz, *IEEE Access*, 2021, **9**, 77493-77510.
16. J. Singh, R. Kaur and D. Singh, *International Journal of Energy Research*, 2021, **45**, 118-140.
17. R. Yang, Y. Qin, L. Dai and Z. L. Wang, *Nature nanotechnology*, 2009, **4**, 34.
18. M. Grätzel, *nature*, 2001, **414**, 338-344.
19. X. Wang, J. Song, J. Liu and Z. L. Wang, *Science*, 2007, **316**, 102-105.
20. Y. Jia, Y. Pan, C. Wang, C. Liu, C. Shen, C. Pan, Z. Guo and X. Liu, *Nano-Micro Letters*, 2021, **13**, 1-12.
21. G. J. Snyder and E. S. Toberer, in *materials for sustainable energy: a collection of peer-reviewed research and review articles from Nature Publishing Group*, World Scientific, 2011, pp. 101-110.
22. Z.-H. Lin, Y. Yang, J. M. Wu, Y. Liu, F. Zhang and Z. L. Wang, *The journal of physical chemistry letters*, 2012, **3**, 3599-3604.
23. Y. Yang, G. Zhu, H. Zhang, J. Chen, X. Zhong, Z.-H. Lin, Y. Su, P. Bai, X. Wen and Z. L. Wang, *ACS nano*, 2013, **7**, 9461-9468.
24. Z. Liu, C. Liu, Z. Chen, H. Huang, Y. Liu, L. Xue, J. Sun, X. Wang, P. Xiong and J. Zhu, 2023.
25. L. Li, S. Feng, Y. Bai, X. Yang, M. Liu, M. Hao, S. Wang, Y. Wu, F. Sun and Z. Liu, *Nature Communications*, 2022, **13**, 1043.
26. R. Zhang, S. Wang, M. H. Yeh, C. Pan, L. Lin, R. Yu, Y. Zhang, L. Zheng, Z. Jiao and Z. L. Wang, *Advanced Materials*, 2015, **27**, 6482-6487.
27. J. Yin, J. Zhou, S. Fang and W. Guo, *Joule*, 2020, **4**, 1852-1855.
28. J. Feng, M. Graf, K. Liu, D. Ovchinnikov, D. Dumcenco, M. Heiranian, V. Nandigana, N. R. Aluru, A. Kis and A. Radenovic, *Nature*, 2016, **536**, 197.
29. J. Osterle, *Applied Scientific Research, Section A*, 1964, **12**, 425-434.
30. D. Burgreen and F. Nakache, *J. Appl. Mech.*, 1965, **32**, 675-679.
31. J. Yang, F. Lu, L. W. Kostiuk and D. Y. Kwok, *Journal of Micromechanics and Microengineering*, 2003, **13**, 963.
32. P. Král and M. Shapiro, *Physical review letters*, 2001, **86**, 131.
33. S. Ghosh, A. Sood and N. Kumar, *Science*, 2003, **299**, 1042-1044.
34. J. Liu, L. Dai and J. W. Baur, *Journal of applied physics*, 2007, **101**, 064312.
35. P. Dhiman, F. Yavari, X. Mi, H. Gullapalli, Y. Shi, P. M. Ajayan and N. Koratkar, *Nano letters*, 2011, **11**, 3123-3127.
36. W. Guo, C. Cheng, Y. Wu, Y. Jiang, J. Gao, D. Li and L. Jiang, *Adv. Mater.*, 2013, **25**, 6064-6068.
37. G. Xue, Y. Xu, T. Ding, J. Li, J. Yin, W. Fei, Y. Cao, J. Yu, L. Yuan and L. Gong, *Nature nanotechnology*, 2017, **12**, 317-321.
38. T. Ding, K. Liu, J. Li, G. Xue, Q. Chen, L. Huang, B. Hu and J. Zhou, *Advanced Functional Materials*, 2017, **27**, 1700551.
39. F. Zhao, H. Cheng, Z. Zhang, L. Jiang and L. Qu, *Advanced Materials*, 2015, **27**, 4351-4357.
40. F. Zhao, Y. Liang, H. Cheng, L. Jiang and L. Qu, *Energy & Environmental Science*, 2016, **9**, 912-916.
41. Y. Lu, H. Wu, Q. Yang, J. Ping, J. Wu and J. Liu, *Adv. Sustainable Sys,*, 2019, 1900012.
42. X. Gao, T. Xu, C. Shao, Y. Han, B. Lu, Z. Zhang and L. Qu, *J. Mater. Chem. A*, 2019, **7**, 20574-20578.
43. J. Yin, X. Li, J. Yu, Z. Zhang, J. Zhou and W. Guo, *Nature nanotechnology*, 2014, **9**, 378-383.
44. J. Yin, Z. Zhang, X. Li, J. Yu, J. Zhou, Y. Chen and W. Guo, *Nature communications*, 2014, **5**, 1-6.

45. B. Ji, N. Chen, C. Shao, Q. Liu, J. Gao, T. Xu, H. Cheng and L. Qu, *Journal of Materials Chemistry A*, 2019, **7**, 6766-6772.
46. M. Kaur, S. Ishii, S. L. Shinde and T. Nagao, *ACS Sustainable Chemistry & Engineering*, 2017, **5**, 8523-8528.
47. Z. H. Lin, G. Cheng, S. Lee, K. C. Pradel and Z. L. Wang, *Advanced Materials*, 2014, **26**, 4690-4696.
48. Z. H. Lin, G. Cheng, L. Lin, S. Lee and Z. L. Wang, *Angewandte Chemie International Edition*, 2013, **52**, 12545-12549.
49. S. Lin, X. Chen and Z. L. Wang, *Chemical Reviews*, 2021, **122**, 5209-5232.
50. M. Kaur, S. Ishii, R. Nozaki and T. Nagao, *Scientific reports*, 2021, **11**, 1-10.
51. M. Kaur and T. Nagao, *Energy & Fuels*, 2022, **36**, 11443-11456.
52. Z. L. Wang, *Journal*, 2012.
53. M. R. Das, J. M. Borah, W. Kunz, B. W. Ninham and S. Mahiuddin, *Journal of Colloid and Interface Science*, 2010, **344**, 482-491.
54. F. H. van der Heyden, D. Stein and C. Dekker, *Physical review letters*, 2005, **95**, 116104.
55. F. H. van der Heyden, D. J. Bonthuis, D. Stein, C. Meyer and C. Dekker, *Nano letters*, 2007, **7**, 1022-1025.
56. H.-C. Ho, K. Chen, T. Nagao and C.-H. Hsueh, *The Journal of Physical Chemistry C*, 2019, **123**, 21103-21113.
57. O. Saber and H. M. Gobara, *Egyptian Journal of Petroleum*, 2014, **23**, 445-454.
58. L.-B. Huang, W. Xu, C. Zhao, Y.-L. Zhang, K.-L. Yung, D. Diao, K. H. Fung and J. Hao, *ACS applied materials & interfaces*, 2020, **12**, 24030-24038.
59. M. Mariello, E. Scarpa, L. Algieri, F. Guido, V. M. Mastronardi, A. Qualtieri and M. De Vittorio, *Energies*, 2020, **13**, 1625.
60. A. Bard, *Standard potentials in aqueous solution*, Routledge, 2017.
61. Z. Lin and Z. Yang, *Droplet*, e97.
62. W. Xu, H. Zheng, Y. Liu, X. Zhou, C. Zhang, Y. Song, X. Deng, M. Leung, Z. Yang and R. X. Xu, *Nature*, 2020, **578**, 392-396.